Tectonophysics 813 (2021) 228913

Contents lists available at ScienceDirect

Tectonophysics

journal homepage: www.elsevier.com/locate/tecto

Imaging the shallow crustal velocity structure of the Qingchengzi ore field on the Liaodong Peninsula, China, with a short-period dense array using ambient noise tomography

Tongtong Xie [a,b], Tao Xu [a,c,*], Yinshuang Ai [c,d], Qingdong Zeng [c,e,f], Wei Zhang [g], Fan Zheng [a,b]

[a] State Key Laboratory of Lithospheric Evolution, Institute of Geology and Geophysics, Chinese Academy of Sciences, Beijing 100029, China
[b] University of Chinese Academy of Sciences, Beijing 100049, China
[c] Innovation Academy for Earth Science, Chinese Academy of Sciences, Beijing 100029, China
[d] Key Laboratory of Earth and Planetary Physics, Institute of Geology and Geophysics, Chinese Academy of Sciences, Beijing 100029, China
[e] Key Laboratory of Mineral Resources, Institute of Geology and Geophysics, Chinese Academy of Sciences, Beijing 100029, China
[f] College of Earth and Planetary Sciences, University of Chinese Academy of Sciences, Beijing 100049, China
[g] Department of Earth and Space Sciences, Southern University of Science and Technology, Shenzhen 518055, China

ARTICLE INFO

Keywords:
Qingchengzi ore field
Gold mineralization
Shallow crustal velocity structure
Short-period dense array
Ambient noise tomography

ABSTRACT

The Qingchengzi ore field, which is located in the middle of the Liaodong Peninsula, has a large number of Au, Ag, and Pb-Zn deposits owing to Mesozoic tectonic and magmatic-hydrothermal activities. To reveal the relationship between shallow crustal velocity and gold mineralization and provide constraints on deep ore prospecting (> 1.5 km), ambient noise tomography consisting of an experimental short-period dense array with 334 seismographs surrounding the study region, is adopted. Shallow crustal velocities at depths less than 5.0 km are obtained by a direct inversion method of Rayleigh wave phase velocity dispersion at a period of 0.5–3.0 s. We obtain the following results. (1) The Jianshanzi fault (JSZF) is well imaged at a depth of 5.0 km. Because ore-forming fluids and materials originated from adjacent concealed granite intrusions characterized by low-velocity anomalies, we infer that the JSZF contributed to mineralization. (2) The Baiyun gold alteration belt in the northern ore field has a high velocity and cuts through the surrounding low-velocity area, extending downward to approximately 0.9 km. This high-velocity belt may be a superposition of the marble of the Dashiqiao Formation and mineralization-alteration, which suggests that the depth of the belt may be of favorable prospecting potential. (3) Based on the obvious low-velocity intrusive anomalies beneath the southern Xiaotongjiapuzi gold belt, we deduce that the mineralization of the Xiaotongjiapuzi gold belt is controlled by unexposed granite intrusions and thus has high mineralization potential at great depths. (4) A geologically reasonable model of the distribution of possible concealed granite intrusions related to deep mineralization and two prospective mineralization areas is presented.

1. Introduction

The Liaodong Peninsula, an important gold-polymetallic district, is located in the northeastern North China Craton (NCC). During the Mesozoic Era, the tectonic environment of the lithosphere underwent a transition from compressional orogenesis to extensional thinning (Yang et al., 2004; Yang et al., 2008; Lin et al., 2011), which triggered strong tectonic and magmatic activities, accompanied by intense gold mineralization (Yang et al., 2003; Wu et al., 2005a; Wu et al., 2005b; Zhu et al., 2015; Zhu and Sun, 2021). Since the 1950s, a number of medium- to large-scale gold-polymetallic ore fields on the Liaodong Peninsula have been explored, such as the Qingchengzi, Wulong, and Maoling ore fields in Fig. 1 (Di et al., 2020). In this paper, we focus on the Qingchengzi ore field located in the center of the Liaodong area. Cumulatively, more than 1.6 million tons of Pb-Zn resources, 300 tons of Au resources, and 4000 tons of Ag resources have been discovered in this ore field (Wang et al., 2017).

To date, many basic geological studies have been performed (Sun

* Corresponding author at: State Key Laboratory of Lithospheric Evolution, Institute of Geology and Geophysics, Chinese Academy of Sciences, Beijing 100029, China.
E-mail address: xutao@mail.iggcas.ac.cn (T. Xu).

https://doi.org/10.1016/j.tecto.2021.228913
Received 26 September 2020; Received in revised form 20 April 2021; Accepted 29 April 2021
Available online 12 May 2021

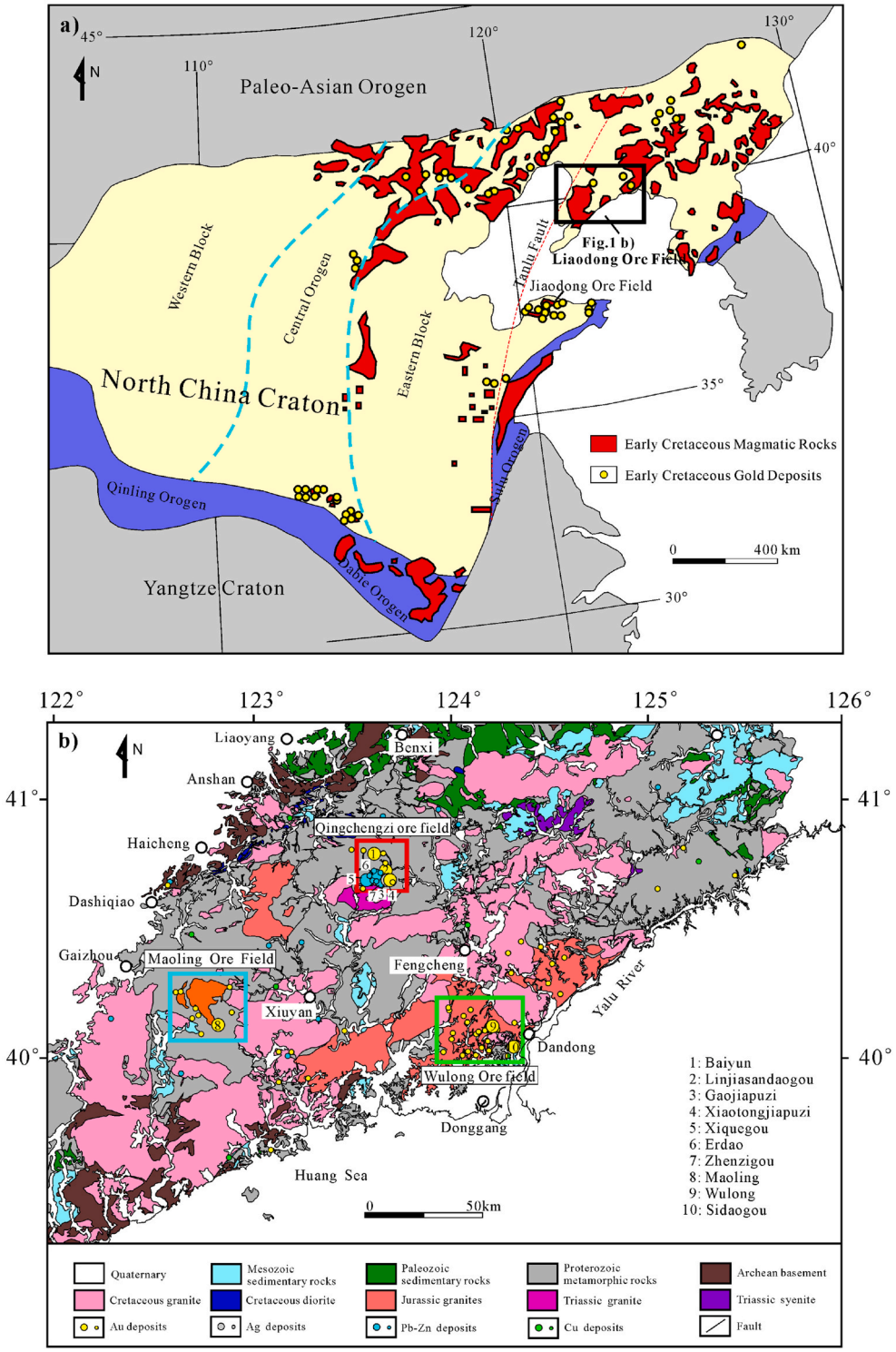

Fig. 1. Geological map and main ore fields of the Liaodong Peninsula (modified from Zeng et al., 2019). a) Tectonic background of the North China Craton. The black rectangular box marks the Liaodong Peninsula (Fig. 1b). b) Geological map and main ore fields of the Liaodong Peninsula. There are three main ore fields on the Liaodong Peninsula. The blue-, red-, and green- rectangular boxes represent the Maoling, Qingchengzi and Wulong ore fields, respectively. (For interpretation of the references to colour in this figure legend, the reader is referred to the web version of this article.)

et al., 1997; Liu and Ai, 1999, 2000; Xue et al., 2003; Liu et al., 2007; Yu et al., 2009; Wang et al., 2010; Duan et al., 2014; Wang et al., 2014; Duan et al., 2017; Hao et al., 2017; Wang et al., 2017; Zeng et al., 2019). These works generally investigated the geological characteristics and prospecting indicators of mineral deposits in the Qingchengzi ore field. Although the genesis of gold deposits is still under debate (Sun et al., 1997; Xue et al., 2003; Liu and Ai, 2000), there is a consensus that these deposits are all granitoid-related and have a magmatic origin. The latest research shows that the genesis of the gold deposits in the Qingchengzi ore field is magmatic-hydrothermal, related to Early Cretaceous granitoid intrusions, and controlled by fault systems (Sun et al., 2019; Sun et al., 2020).

The spatial distribution and dynamic mechanism of gold deposits in the Qingchengzi ore field, which are important to regional mineral prospecting, can be investigated with 3D structural images. Recently, a variety of geophysical methods have been applied for mineral exploration in this area. The aeronautical magnetotelluric method has inferred and explained the distribution characteristics of rock masses and ore-controlling structures in this area with differences in permeability and conductivity of underground media (Wang et al., 2020). Based on

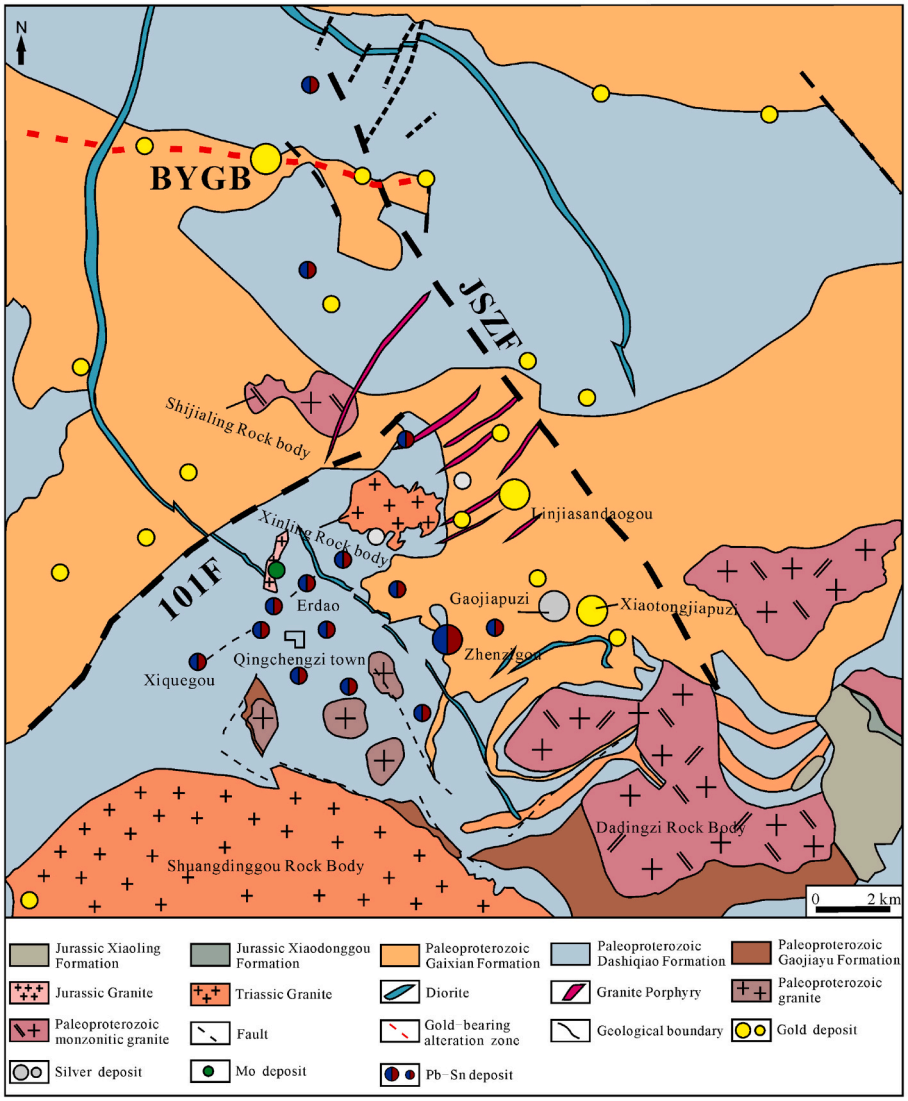

Fig. 2. Geological map of the Qingchengzi ore field (modified from Zeng et al., 2019). The black dashed lines show two main faults in the study area: the Jianshanzi Fault (JSZF) and 101 Fault (101F). The red dashed line represents the Baiyun gold belt (BYGB). The yellow circles denote major gold deposits. (For interpretation of the references to colour in this figure legend, the reader is referred to the web version of this article.)

gravity-magnetic anomalies, the relationship between rock densities, resistivities, and mineralization can be studied (Di et al., 2020; Wu et al., 2020; Yang, 2019). Due to the inherent limitations, such as shallow resolution depth, geometry limitations, and high cost, of the above-mentioned methods, the Qingchengzi ore field is poorly constrained at depths greater than 1.5 km, although surface geological observations indicate that the Qingchengzi ore field is very promising for discovering additional gold mineralization at depths greater than 1.5 km (Di et al., 2020). Therefore, for deep mineralization prospecting, it is necessary to adopt methods capable of imaging the deep earth that provide deeper data at a higher resolution and less cost, which are key ingredients for achieving future exploration success (Zeng et al., 2019). For this reason, we adopt a seismological method to investigate the 3D shallow crustal velocity in the Qingchengzi ore field in this paper.

In recent years, short-period dense array imaging technology has gained growing importance in investigating fine earth structures, and this technology can meet the requirements of shallow crustal velocity imaging in the Qingchengzi ore field (Lin et al., 2013; Schmandt and Clayton, 2013; Nakata et al., 2015; Chang et al., 2016; Roux et al., 2016; Liu et al., 2017a; Liu et al., 2017b; Bao et al., 2018; Wei et al., 2018; Mordret et al., 2019). With the dense coverage of a station array, the ambient noise tomography method, a feasible, cost-effective, and environmentally friendly method (Du et al., 2020), has been recently applied to related shallow crustal studies, such as volcano monitoring (e.g. Li et al., 2016), sedimentary basins (Huang et al., 2010; Fang et al., 2015; Wang et al., 2018), hydrocarbon reservoirs (Mordret et al., 2013; Mordret et al., 2014; Chmiel et al., 2016; Chmiel et al., 2019), and mineralization exploration (Hollis et al., 2019; Du et al., 2020; Lavoué et al., 2020; Yu et al., 2020; Zhang et al., 2021). In the Xinjiang Basin in southeastern China, Wang et al. (2018) deployed 203 short-period seismographs at a spacing of ~400 m and obtained a high-resolution velocity structure at depths of 0–1.4 km with more than 16,000 Rayleigh wave phase velocity dispersion curves at periods of 0.2–1.7 s. Based on the Valhall Life of Field Seismic network that has 2320 sensors deployed on the seafloor of the North Sea, Mordret et al. (2014) computed over 2,600,000 cross-correlations of 6.5-h vertical component noise data; in addition, using phase and group dispersion curves at periods between 0.6 and 1.6 s, they imaged the high-resolution 3D subsurface at 600 m by a neighborhood algorithm-based depth inversion method, which can be applied to monitor seafloor subsidence due to oil extraction. Above the Groningen gas field in Europe, to monitor the seismic activity and gas field, Chmiel et al. (2019) deployed four flexible

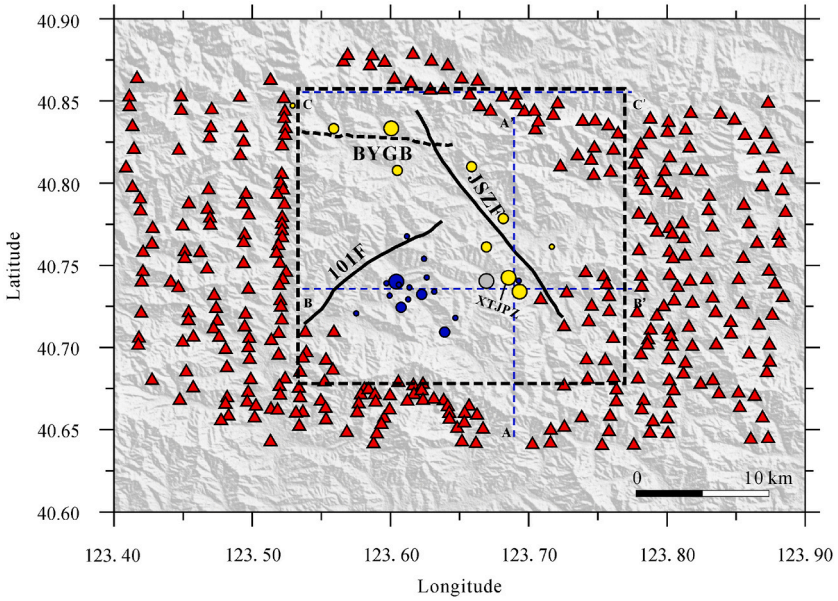

Fig. 3. Station locations in the Qingchengzi ore field. Red triangles represent the location of the seismic array. The dotted rectangle denotes the region of the Qingchengzi ore field. Lines A-A′, B-B′, and C-C′ are the profiles for the analysis of inversion results (Fig. 10). (For interpretation of the references to colour in this figure legend, the reader is referred to the web version of this article.)

networks for ~1 month with approximately 400 sensors in each data block. By a joint inversion of Rayleigh and Love wave dispersion curves within periods of 0.6–4.2 s, the detailed shear wave velocity structure reaching 1.0 km beneath the four gas areas was determined.

For mineralization exploration, deposits have been studied from different perspectives, including the structure and geometry of ore-bearing formations, the sources of ore-forming heats and materials, and the ore-controlling fault systems. At the Marathon PGM-Cu deposit, in Ontario, Canada, Hollis et al. (2019) obtained a 3D shallow crustal velocity structure at depths reaching 1.5 km by jointly inverting the Rayleigh wave phase and group dispersion curves at short periods of 0.1–1.2 s and 0.15–1.5 s, which revealed that the mineralization related gabbro intrusion slab is a higher velocity layer and dips toward the west. Du et al. (2020) obtained a 3D velocity structure at a depth of 0–1.3 km beneath the Karatungk Cu-Ni mine in Xinjiang, western China, with Rayleigh wave dispersion curves of 0.1–1.5 s and data recorded by 100 single-component seismometers. Velocity anomalies related to the major ore-hosting intrusions at depths 0–0.7 km and the source regions of these ore-hosting intrusions at deeper depth (0.7–1.3 km) were presented. Yu et al. (2020), using a linear array consisting of 340 short-period seismograms with an average interval of 0.5 km, investigated the significance of extensional structure and gold mineralization on the Jiaodong Peninsula, eastern NCC. With Rayleigh wave phase velocity dispersion curves at periods of 0.5–4.0 s, they obtained a shallow velocity profile at depths less than 8.0 km and demonstrated that gold mineralization differences on the western and eastern Jiaodong Peninsula are mainly caused by different ore-controlling fault systems.

In this paper, to reveal the relationship between shallow crustal velocity and gold mineralization and provide constraints on deep ore prospecting (> 1.5 km), we deployed an experimental short-period dense array with 334 three-component seismometers surrounding the study region and applied the ambient noise tomography method. Following a well-established workflow (Yao et al., 2006; Bensen et al., 2007; Yao et al., 2008), we obtain 17,425 Rayleigh wave phase velocity dispersion curves at periods of 0.5–3.0 s. Based on the collected dispersion curves, a direct surface wave tomography method (Fang et al., 2015) is adopted to obtain the shallow velocity structure at depths of 0.5–5.0 km beneath the study area. We further analyze the velocity anomalies related to the lithology and stratigraphy, concealed granite intrusions, and fault structure, which provide geophysical constraints on the gold mineralization at great depths in the Qingchengzi ore field.

2. Geological setting

The Qingchengzi district is a Pb-Zn-Au-Ag polymetallic ore field located in the center of the Liaodong area. The strata in this ore field are mainly the Paleoproterozoic Liaohe Group, which contains, from bottom to top, the Gaojiayu, Dashiqiao, and Gaixian Formations (Fms.) (Fig. 2). The Gaixian Fm. is mainly composed of mica schist, sillimanite-mica schist, garnet-mica schist, and marble-bearing tremolite schist. The Dashiqiao Fm. is mainly composed of dolomitic marble, mica-strip marble, granulite-bearing tremolite marble, garnet-mica schist, and sillimanite-mica schist. Graphite-bearing marble, amphibolite schist, sillimanite mica schist, and marble are the most widely distributed rocks in the Gaojiayu Fm.

Intermediate-acidic intrusions and various dikes are identified in the ore field, including the Paleoproterozoic Dadingzi monzonitic granite, Triassic Shuangdinggou monzonitic granite, Xinling granite porphyry, Yanshanian Yaojiagou granite, northwestward diorite dike, northeastward lamprophyre, and granite porphyry dikes. The zircon U-Pb age of the Dadingzi monzogranite is 1869 ± 16 Ma (Song et al., 2016; Di et al., 2020). The zircon U-Pb age of the Shuangdinggou monzogranite is 224.2 ± 1.2 Ma and the emplacement age of the Xinling granite porphyry is 225.3 ± 1.8 Ma (Yu et al., 2009; Di et al., 2020). The zircon U-Pb age of the Yaojiagou granite is 167.5 ± 0.9 Ma (Zhang et al., 2016; Di et al., 2020).

Two groups of faults occur in the Qingchengzi ore field: one group of faults extends in the NW-SE direction and is represented by the Jianshanzi Fault, and the other group has a NE-SW strike (e.g., the 101 Fault). Some deposits are distributed along these two main faults and their second-order faults, which may be a potential indicator of gold mineralization in this area. Generally, the gold deposits in the Qingchengzi ore field are mainly clustered near three NW-trending belts, namely, the Xiaotongjiapuzi belt, the Baiyun belt, and the Linjiasandaogou belt. These belts contain large-scale gold deposits, such as the Baiyun, Xiaotongjiapuzi, Yangjia, and Linjiasandaogou gold deposits, as well as a series of gold occurrences (Zeng et al., 2019).

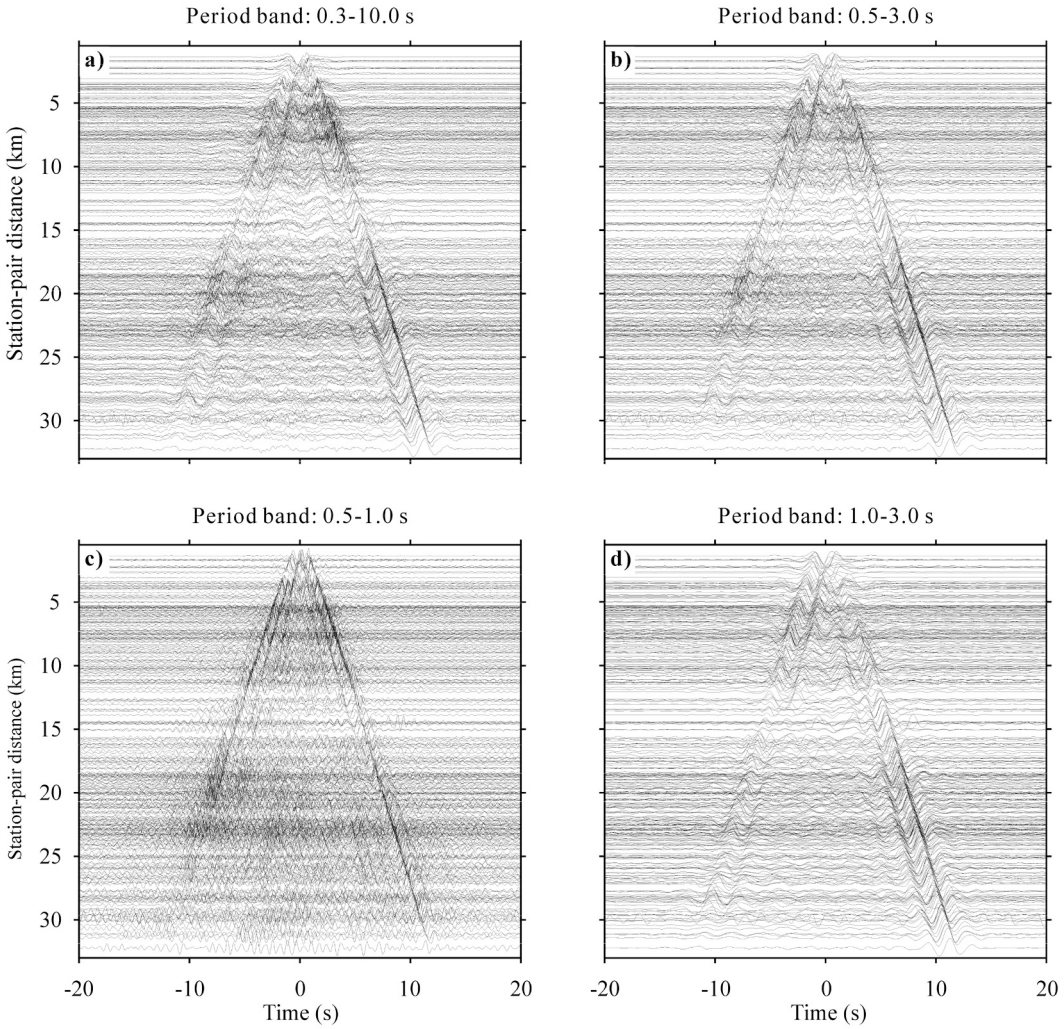

Fig. 4. CCFs between station 0116 and other stations. a) CCFs are originally calculated at a period band of 0.3–10.0 s. The original CCFs are bandpass filtered in three different period bands: b) 0.5–3.0 s, c) 0.5–1.0 s, and d) 1.0–3.0 s.

3. 3D data processing

3.1. Data and imaging method

To obtain the shallow crustal velocity structure and provide constraints on deep ore prospecting (> 1.5 km), in the first phase, we deployed an experimental short-period seismic array surrounding the Qingchengzi ore field (Fig. 3), which is referred to as QSP array-I hereafter. Under the coverage of dense ray paths, this array can provide a transmissive geometry to image the shallow regional velocity structure. QSP array-I consists of 334 three-component (3-C) SmartSolo seismometers with 24 digitizer bits, whose natural frequency is 5 Hz; QSP array-I collected approximately 32 days of continuous ambient noise recordings from approximately 8 June to 10 July 2019, with an average station spacing of ~1 km and an original sampling frequency of 250 Hz. Of the two groups of faults in the study region, one group of faults strikes in the NW-SE direction, and the other strikes in the NE-SW direction. We have installed more stations in the W-E direction to cover the fault distribution.

In this paper, ambient noise tomography with vertical component data is applied. Using an image transformation technique under a far-field approximation (Yao et al., 2006; Yao et al., 2008), the time-domain empirical Green's functions (EGFs) can be first estimated from the negative time derivative of the long time cross-correlation of ambient seismic noise (Sabra et al., 2005; Campillo et al., 2014); then, the Rayleigh wave phase velocity dispersion curve from the EGFs are extracted. The direct surface wave tomography method is adopted to obtain a shallow complex velocity structure, which is based on a fast marching ray-tracing method (Rawlinson and Sambridge, 2005) and a wavelet-based sparsity-constrained inversion technique (Fang and Zhang, 2014). This method avoids the assumption of great-circle propagation that is usually used in conventional surface wave tomographic studies, which is not optimal in complex media (Fang et al., 2015).

3.2. Cross-correlation calculation

We first convert the original data format recorded by the SmartSolo seismograph to the SAC data format, and then cut the vertical component data into hourly segments at a sampling rate of 10 Hz. After that, we follow the procedure presented by Bensen et al. (2007) to process the data segments, including instrument response removal, waveform demeaning and detrending, spectral whiting, and temporal one-bit normalization. Finally, the cross-correlation functions (CCFs) of all station pairs at a period band of 0.3–10.0 s are calculated, and the hourly CCFs from each station pair are linearly stacked together to improve the signal-to-noise ratio (SNR).

To determine the effective frequency band of the surface wave signal contained in the CCFs originally calculated (Fig. 4a), we bandpass filter the CCFs at three different period bands (Fig. 4b-d). Generally, the surface wave signals are all clear, and the apparent velocity is

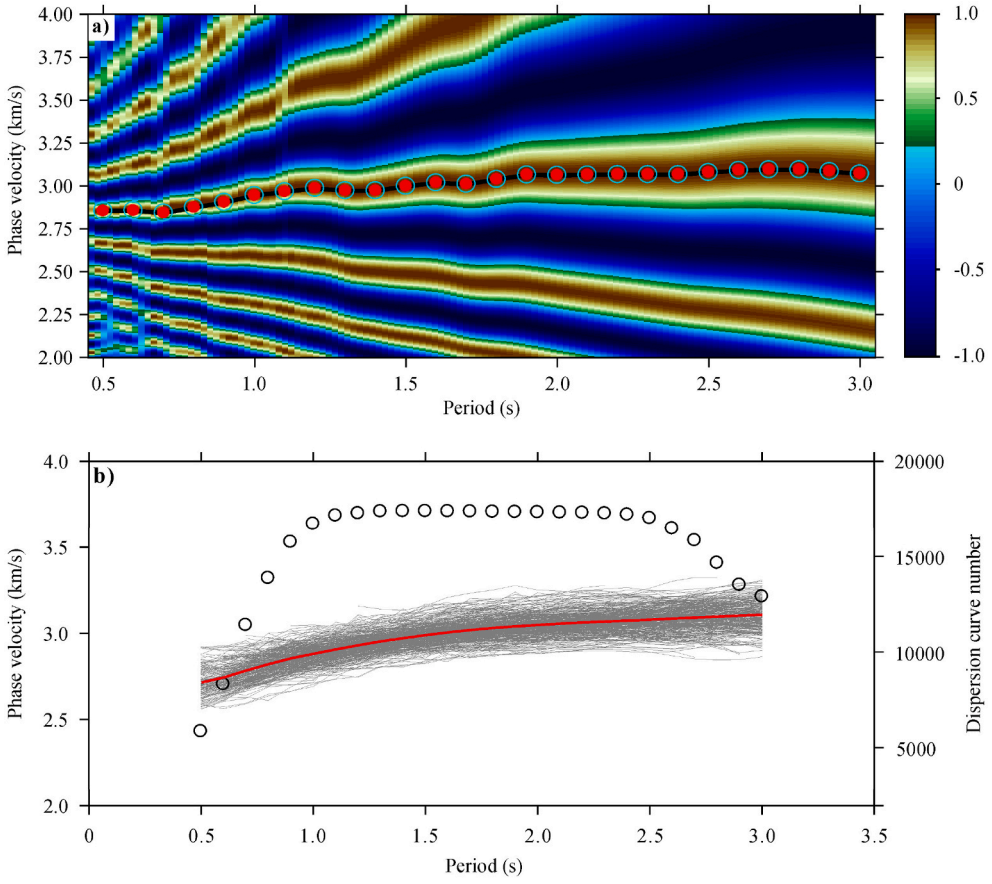

Fig. 5. Phase velocity dispersion extraction. a) An example of extracting phase velocity dispersion curves with the image transformation technique. The colour bar represents the normalized surface wave envelope amplitude. Light blue circles represent dispersion points satisfied with the choice conditions and solid red points are the final reserved dispersion points. b) Phase velocity dispersion curves extracted from the EGFs. The red solid line denotes the average phase velocity dispersion curve of all station pairs. The black circles represent the number of phase velocity dispersion nodes at each period. The gray solid lines show dispersion curves randomly selected. (For interpretation of the references to colour in this figure legend, the reader is referred to the web version of this article.)

approximately 3.0 km/s. The CCFs at the period band of 0.5–3.0 s (Fig. 4b) are nearly the same as those at 0.3–10.0 s, which indicates that the effective period band of the surface wave signal in our dataset is approximately 0.5–3.0 s. The high-frequency CCFs at the period band of 0.5–1.0 s (Fig. 4c) constrain the shallow structure, while the low-frequency CCFs at the period band of 1.0–3.0 s (Fig. 4d) constrain the deep structure, in which the surface wave signal is relatively clear. In general, the effective period band of 0.5–3.0 s carries the majority of surface wave information, which is selected as the period band of phase velocity dispersion curves in the S-wave inversion. Furthermore, the time-frequency transform of a single CCF (Fig. A.1) is analyzed and shows the frequency contents of surface waves at different travel times, which is consistent with our conclusions above.

3.3. Phase velocity dispersion extraction

Theoretically, we can extract 55,611 Rayleigh wave phase velocity dispersion curves from 334 seismic stations. When considering the distribution of seismic stations, the interstation spacing along the N-S direction is smaller than that along the E-W direction; in addition, the number of station pairs along the N-S direction is also less than that along the E-W direction. Thus, we first extract the dispersion curves of station pairs with interstation distances larger than 25.0 km to satisfy the far-field approximation, and then we add dispersion curves corresponding to station pairs with interstation distances less than 25.0 km distributed along the N-S direction to ensure an approximate uniform distribution of ray paths along both directions.

Using the image transformation technique (Yao et al., 2006; Yao et al., 2008), after inputting the CCFs, the EGFs are first estimated from the negative time derivative of the CCFs (Sabra et al., 2005; Campillo et al., 2014); then, to suppress the effect of the uneven distribution of ambient seismic noise sources, the positive and negative time lags of EGFs are linearly stacked. The phase velocity dispersion curves within the 0.5–3.0 s period band are finally extracted based on symmetric component EGFs with a time interval of 0.1 s (Fig. 5a). We select EGFs with an interstation distance of at least two wavelengths to satisfy the far-field approximation and with a SNR $>$ 5 to obtain high-quality dispersion data. In addition, we also remove a few outlier dispersion nodes in a single dispersion curve with a velocity gradient larger than 0.3 km/s, which is inconsistent with all the other nodes due to low SNRs of CCFs (Fig. A.2), to obtain smooth dispersion curves for geological rationality. Finally, we reserve only dispersion curves with a velocity range within 5 times the standard deviation of all the phase velocity dispersion curves. Fig. 5b shows the distribution of partial phase velocity dispersion curves randomly selected at the period band of 0.5–3.0 s and the number of phase velocity dispersion nodes at each period.

3.4. 3D shear wave velocity inversion

3.4.1. Direct surface wave tomography method

In this paper, we use the direct 3D surface wave tomography method (Fang et al., 2015) to obtain the shallow crustal structure in the Qingchengzi ore field. Compared to conventional inversion methods (Yao et al., 2006; Yao et al., 2008), this method avoids the intermediate inversion steps of phase or group velocity maps and can consider the ray-bending effects in a complex medium (Fang et al., 2015). At each period, the fast marching method is adopted to compute surface wave travel times and ray paths between sources and receivers (Rawlinson and Sambridge, 2005). Based on the phase velocity dispersion data, the 3D shear wave velocity model is parametrized by means of 1D profiles beneath grid points using the wavelet-based sparsity-constrained tomographic method (Fang and Zhang, 2014; Fang et al., 2015) and is updated by an iteratively reweighted least-squares algorithm. The objective function is defined by minimizing the difference between the

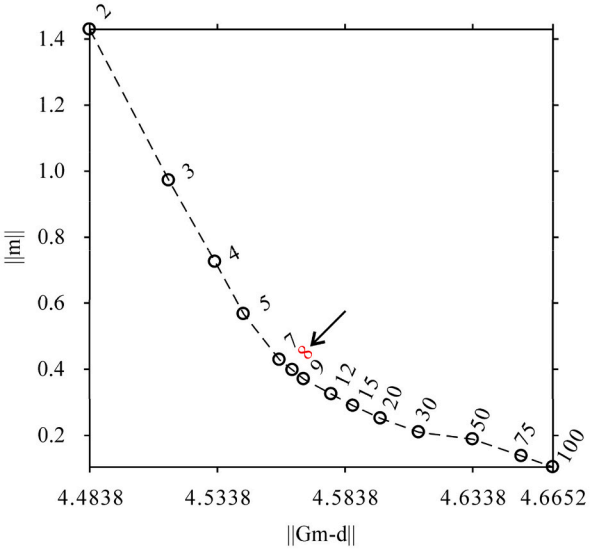

Fig. 6. L-curve obtained from different λ values. The best value is 8 as indicated by the black arrow.

model prediction times and the observed times,

$$\Phi(\mathbf{m}) = \|\mathbf{d} - \mathbf{Gm}\|_2^2 + \lambda\|\mathbf{Lm}\|_2^2$$

where **d** is the surface wave travel time residual vector for given paths and frequencies, **G** is the data sensitivity matrix, **m** is the model parameter vector, **L** is a model smoothing operator, and λ is a weighting parameter that balances data fitting and model regularization (Fang et al., 2015).

3.4.2. *Weighting parameter determination*

As mentioned above, λ is a key parameter that balances data misfit and model smoothness. If λ is too small, the inversion procedure may be unstable and easily sensitive to noise; in contrast, the result is over-smoothing and poorly resolved (Lo et al., 2019). When the noise level in the data is known, λ can be determined from the discrepancy principle (Scherzer, 1993). However, the data noise is usually unknown, as in seismic tomography. In this case, λ can be derived from generalized cross-validation or the L-curve method (Fang et al., 2015). In this paper, we test different λ values and take 8, the corner value of the L-curve, as the best value (Fig. 6).

3.4.3. *Checkerboard resolution test*

The checkerboard resolution test is an effective way to check the coverage of ray path, and it can provide a reference anomaly size that can be trusted for a given geometry. The recovery ability of checkerboards depends primarily on ray-path coverage. In this paper, the coverage of ray paths generated by the transmissive geometry is dense and homogeneous at different periods, as shown in Fig. 7. Then, we perform checkerboard resolution tests to evaluate both the lateral and vertical resolution. The 3D background velocity model is constructed based on the principle that the fundamental mode Rayleigh wave phase velocity is most sensitive to shear wave velocity at depths of approximately one-third of its corresponding wavelength. For a uniform half-space Poisson solid, the phase velocity is equal to 0.92 times the shear wave velocity (Shearer, 2019). Thus, we use 1.1 times the average measured phase velocities at a depth of 1/3 times the wavelength as the background velocity model (Fang et al., 2015). The study region is parameterized by 0.015° × 0.017° grid points. Using a background velocity model (see section 4), we first generate real checkerboard models by adding velocity perturbation to the background velocity model. Then, based on the known locations of station pairs and checkerboard models, the synthetic phase velocity of the Rayleigh wave is obtained by a forward method proposed by Dunkin (1965) and Herrmann (2001). Finally, we apply the direct surface wave tomography method to the synthetic data to recover the real checkerboard models with the background velocity model as the initial mode.

For the lateral resolution test, the anomaly size is approximately 0.040° × 0.040°, and the velocity perturbation is ±0.3km/s of the background velocity. The recovery results of the lateral checkerboard resolution test at different depths are shown in Fig. 8. For vertical resolution tests, the anomaly size is approximately 0.8 km along the vertical direction, and the velocity perturbation is ±0.3km/s of the background velocity. The surface locations and the inverted results of vertical profiles M-M' and N-N′ are shown in Fig. A.3.

At the edges of the study region, where the ray-path coverage is poor, the checkerboards are poorly recovered. In the center of the study region, both the lateral and vertical checkerboard tests are well recovered with a dense ray-path coverage. The whole Qingchengzi ore field is well recovered with anomalies as small as approximately 0.040° in the lateral direction and approximately 0.8 km in the vertical direction. Horizontal slices at depths less than 5.0 km are reliably resolved within the region of the large gray dotted rectangle (Fig. 8).

For the vertical profile, the imaging depth and resolution are constrained by the surface wave period. The imaging depth increases as the surface wave period increases, while the vertical resolution decreases as the surface wave period increases, which results in a poorer resolution at deeper depths. In this paper, the Rayleigh wave phase velocity dispersion curves are extracted at a period of 0.5–3.0 s and with fewer numbers along the N-S direction. Therefore, we consider only the vertical models at depths of 0.4–3.0 km and anomalous body sizes of approximately 0.8 km that are well recovered, which can be used for further discussion and interpretation based on checkerboard tests (Fig. A.3).

4. Inversion results

In the inversion, we adopt the same initial shear wave velocity model as that of the background velocity model in the checkerboard resolution test. The depth of the initial model is extended to 15.0 km to avoid boundary effects and stabilize the inversion (Yu et al., 2020). The velocity model at depths of 0.5–3.5 km is constructed by linearly interpolating 1.1 times the average phase velocity. We fix the shear wave velocity as 3.6 km/s below 7.0 km and linearly interpolate the velocity between depths of 3.5 km and 7.0 km. The velocity at 0 km is obtained by linearly extrapolating the velocity curve to the surface. We parameterize the study region by 0.015° × 0.017° grid points and take the weighting parameter as 8 based on the L-curve test. The inversion iterates 10 times. Shallow crustal shear wave velocity slices at different depths are shown in Fig. 9. The shear wave velocities of profiles A-A', B-B′, and C-C′ in Fig. 3 are shown in Fig. 10.

We also show the initial and final average travel time residuals in Fig. 11. Compared with the initial average travel time residuals (0.0325), the final average travel time residuals (0.0047) have been largely decreased, which demonstrates that the final velocity model fits the observed data better.

4.1. *Stability tests based on different initial models*

To test the dependence of the inversion results on the initial models and obtain the maximum average convergence depth, we repeat the inversion process based on two groups of initial models.

The first group of initial velocity models (Fig. 12a) is generated from the phase velocity dispersion curves by considering prior information. These models include the initial velocity model used by the direct inversion in section 4 (blue lines in Fig. 12a), the linear velocity model (black lines in Fig. 12a), and the linear velocity model plus low- and high-velocity anomalies at depths of 1.2–2.4 km (red lines in Fig. 12a). The second group of initial velocity models (Fig. 12b) is based on the

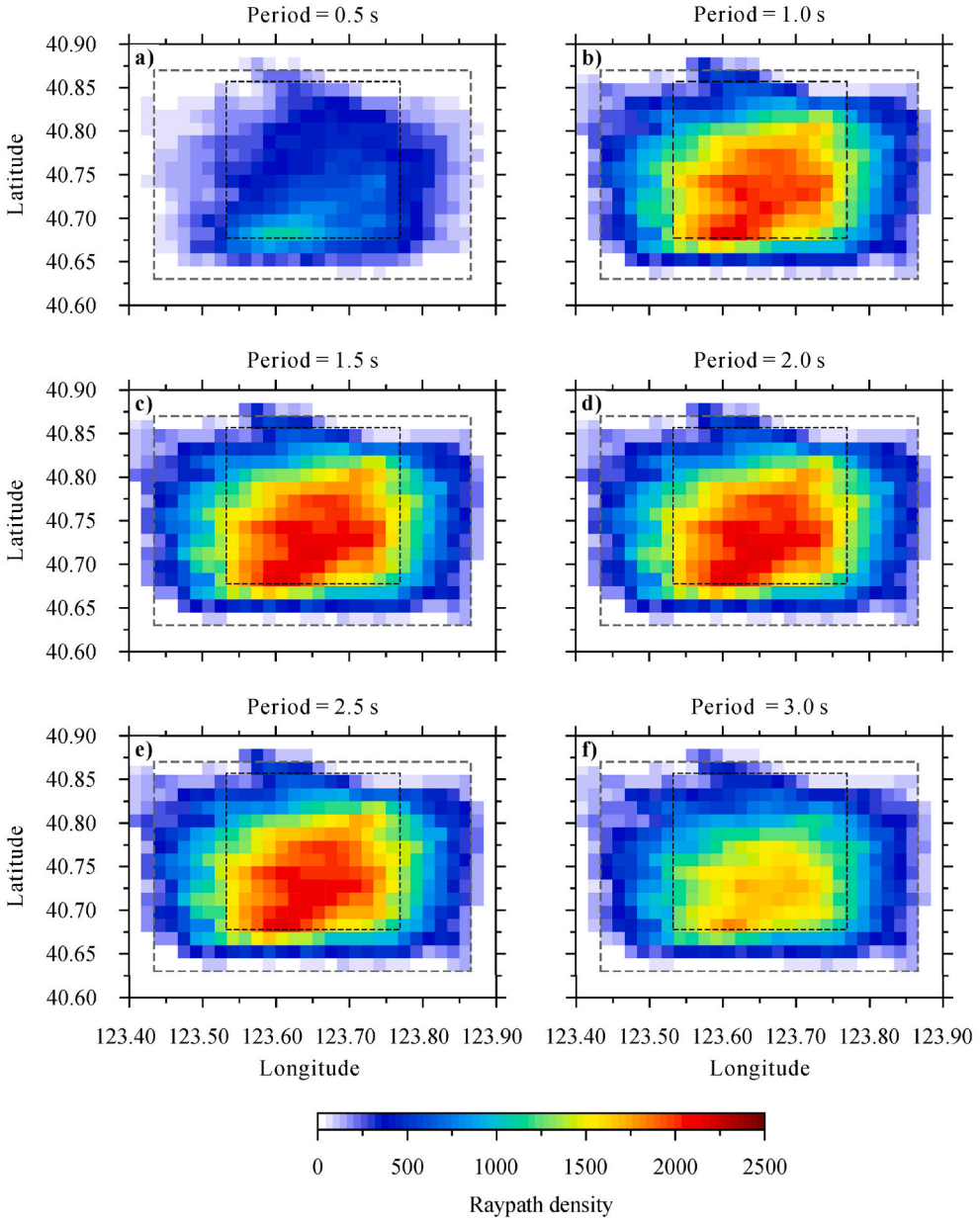

Fig. 7. The density of ray-path coverage at periods of 0.5 s, 1.0 s, 1.5 s, 2.0 s, 2.5 s, and 3.0 s. The small black dotted rectangle denotes the region of the Qingchengzi ore field. The large gray dotted rectangle represents the regions, in which ray paths are well covered.

linear initial velocity models with one or two velocity gradients generated without prior information (black lines in Fig. 12b), and then the velocity models are shifted systematically to generate another two subgroups: higher (blue lines in Fig. 12b) and lower (red lines in Fig. 12b) initial velocity models.

For the two groups of initial velocity models, we calculate both the average velocities of the output models at each depth within the reliable regions (the large gray dotted rectangle in Fig. 9) and then compare them with those of the initial models in each group. Thus, we obtain the maximum average convergence depth of the vertical profile that can be constrained by the two different groups of initial models (Fig. 12c-d). A comparison of the average velocities computed by the inverted models in the two groups shows that the inversion results at depths of approximately 0.4–5.0 km are both relatively convergent and stable, and not greatly affected by the initial velocity models. At greater depths (> 5.0 km), due to the narrow period band (0.5–3.0 s) of the Rayleigh wave phase velocity dispersion in this paper, the inversion results in the second group are relatively divergent and less constrained, whose initial velocity models are without prior information and inaccurate. For the first group of initial velocity models with prior information, the inversion results are still convergent at approximately 7.0 km, below which we fix the shear wave velocity as 3.6 km/s. Therefore, the maximum average convergence depth in the inverted velocity model is 7.0 km.

5. Discussion

Based on the ambient noise tomography results, we analyze the velocity anomalies related to the lithology and stratigraphy, concealed granite intrusions, fault structure, and gold mineralization. It is known that the velocity features of imaging results are positively correlated with the lithology densities. In the study region, the average density of the intrusive rock mass is approximately 2.60 g/cm^3 (Niu, 2020), and the low-velocity anomalies numbered 1 to 5 in Fig. 9a-c, are probably granite intrusions. Numbers 1–5 represent low-velocity anomalies

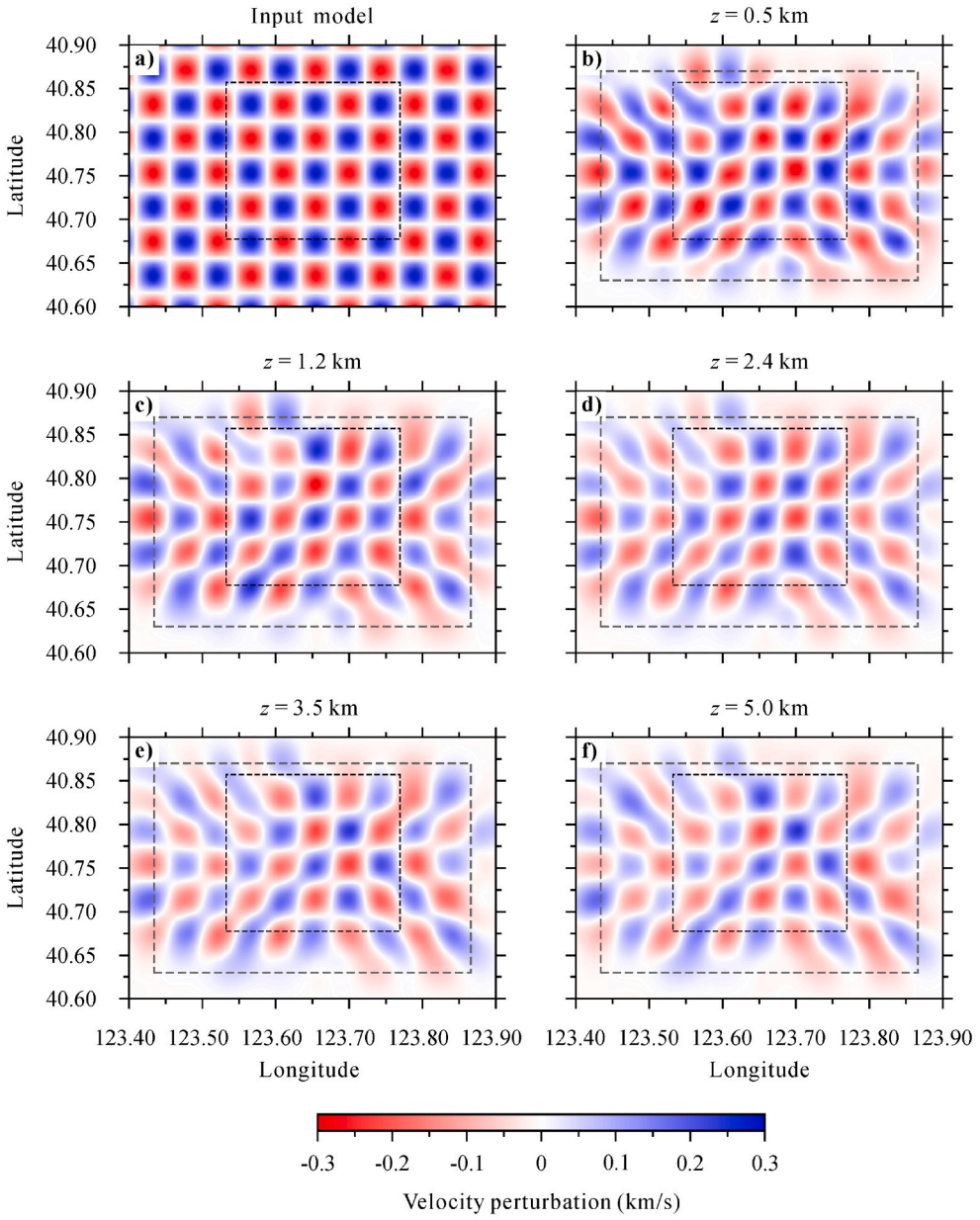

Fig. 8. Lateral checkerboard resolution tests. a) Input checkerboard model, in which the anomaly size is approximately 0.040° × 0.040°. Output model at different depths: b) 0.5 km, c) 1.2 km, d) 2.4 km, e) 3.5 km, and f) 5.0 km. The small black dotted rectangle denotes the region of the Qingchengzi ore field. The large gray dotted rectangle represents the regions, in which checkerboard models are well recovered.

related to the Shijialing rock mass, Sanjiazishan rock mass, Qingchengzi concealed rock mass (see below for details), Shuangdinggou rock mass, and Dadingzi rock mass, respectively. In addition to the low-velocity granite intrusions, the strata in this ore field are mainly the Paleoproterozoic Liaohe Group, which have a relatively high average density of 2.75 g/cm^3 (Niu, 2020) and thereby exhibit high-velocity anomalies.

The Qingchengzi district is a Pb-Zn-Au-Ag polymetallic ore field. The Pb-Zn deposits, denoted as solid blue circles in Fig. 9, are mainly located east of the 101 Fault (101F) and buried in the Paleoproterozoic Dashiqiao Fm. The Au deposits are mainly distributed west of the Jianshanzi Fault (JSZF) (e.g., the Xiaotongjiapuzi gold belt (XTJPZGB) and the Baiyun gold belt (BYGB) in Fig. 9a-c), which is located between the top of the Dashiqiao Fm. and the bottom of the Gaixian Formation. Compared with the XTJPZGB, the velocity anomalies around the areas of the Pb-Zn deposits are relatively low, and a shallow Qingchengzi concealed host stock related to the Pb-Zn deposits may exist (No. 3 in Fig. 9a-c).

As the deposits in the Qingchengzi ore field are all granitoid-related and have a magmatic origin, the potential for deep mineralization (> 1.5 km) is mainly controlled by concealed granite intrusions. For the XTJPZGB in the southern ore field, there are obvious low-velocity anomalies beneath its southern areas (II-c in Figs. 9f-j and 10a-b). Magnetotelluric survey results (Di et al., 2020) also show that there are high apparent resistivity anomalies, which are potential granite intrusions, at depths of ~2.5–8.0 km beneath the southern XTJPZGB. The XTJPZGB is located in a low-to-high-resistivity transition zone, which extends to a significant depth. Thus, we infer that the low-velocity anomaly is a deeply unexposed intrusive granite body that is related to the mineralization of the XTJPZGB. Combined with the magnetotelluric results, we can conclude that the XTJPZGB has great prospecting potential at depths greater than 1.5 km. The BYGB in the northern ore field (Fig. 9a-c), where the gold deposits are generally distributed in the high- and low-velocity transition areas, exhibits a high velocity. The whole high-velocity region (IV in Fig. 9a-c and Fig. 13) cuts the

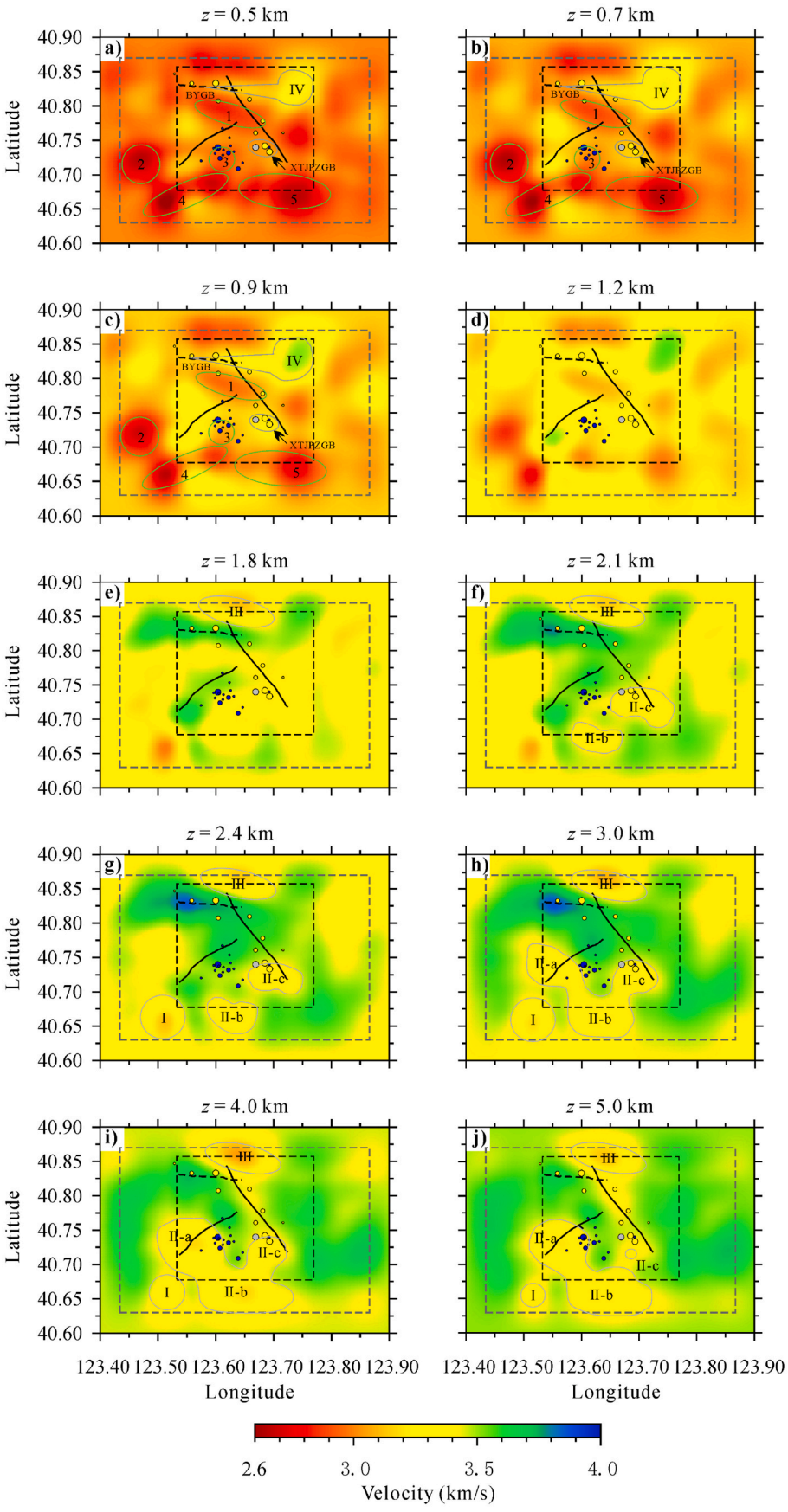

Fig. 9. Shear wave velocity slices at different depths obtained by the direct inversion method: a) 0.5 km, b) 0.7 km, c) 0.9 km, d) 1.2 km, e) 1.8 km, f) 2.1 km, g) 2.4 km, h) 3.0 km, i) 4.0 km, and j) 5.0 km. The small black dotted rectangle denotes the region of the Qingchengzi ore field. The large gray dotted rectangle represents the regions, in which checkerboard models are well recovered. The NW-SE direction black dashed line represents the Jianshanzi Fault (JSZF), and the NE-SW strike is the 101 Fault (101F). The solid blue and yellow circles denote major Pb-Zn and gold deposits. Number 1–5, I -IV and closed curves represent anomalies interpreted in the manuscript. (For interpretation of the references to colour in this figure legend, the reader is referred to the web version of this article.)

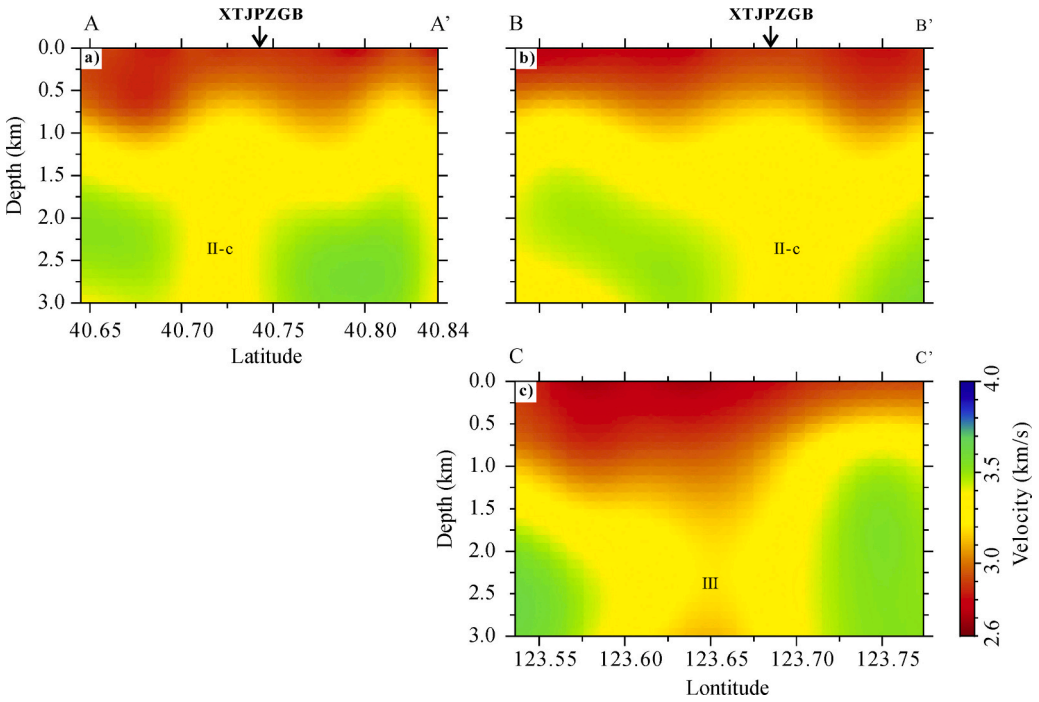

Fig. 10. Shear wave velocity of the selected vertical profiles shown in Fig. 3: a) A-A', b) B-B′, and c) C-C′.

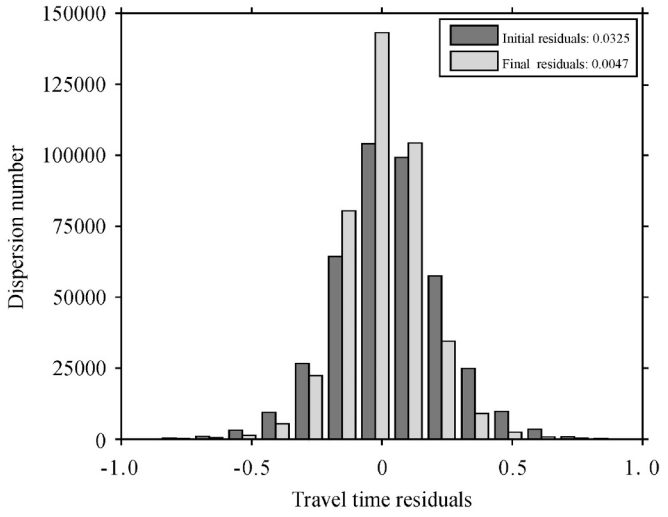

Fig. 11. Histograms of initial and final average travel time residuals. Initial residuals are shown in dark gray, while final residuals are shown in light gray.

surrounding low-velocity areas and extends downward to approximately 0.9 km. Based on previous studies (Zeng et al., 2019; Sun et al., 2020), silicification alteration is a potential indicator of gold mineralization in the BYGB and the alteration width is tens to hundreds of meters. We consider that the BYGB related high-velocity region (IV in Figs. 9a-c and 13) may be the superposition of the marble on the Dashiqiao Fm. (within the whole region) and mineralization-alteration (mainly left sharp part of the region). In addition, north of the BYGB, there is a low-velocity anomaly ranging from 1.8 km to 5.0 km (III in Figs. 9e-j and 10c) that has the same velocity value (3.375 km/s) as low-velocity anomaly II-c, which suggests that concealed granite intrusions related to gold mineralization may exist in the deep part of the northern BYGB. As gold mineralization is often related to concealed granite intrusions, there might be potential gold mineralization at deep depths in the northern BYGB. In addition, other low-velocity anomalies with the same velocity value (3.375 km/s) are present south of the ore field, and are presented as I, II-a, and II-b in Figs. 9f-j and 13, which may also be concealed granite bodies beneath the Shuangdinggou and Dadingzi intrusions.

Due to the relationship of fault systems and mineralization present in the study region, it is obvious that there are many Pb-Zn-Au-Ag deposits distributed between the two main groups of faults and along the JSZF. Previous studies of regional geochemical anomalies show that Au anomalies are distributed along the JSZF (Liu and Ai, 1998, 2002), where a low-velocity anomaly band also exists in our results, as shown in Fig. 9i- j. The low-velocity anomaly band surrounding the JSZF is adjacent to low-velocity anomalies II-c and III, which we deduce to be concealed granite intrusions. We infer that this low-velocity anomaly band may be ore-forming fluids and materials originating from concealed granite intrusions II-c and III that migrated and precipitated along the JSZF and secondary faults on both sides during the mineralization period. Therefore, the JSZF is a large fault at depths as deep as 5.0 km in this study and has great mineralization potential, which is also suggested by magnetotelluric survey results (Di et al., 2020).

In summary, based on the distribution of proven deposits, we analyze the possibilities of related velocity anomalies and further deep mineralization potentials. In addition, considering that gold mineralization is often related to concealed granite intrusions, we also focus on the interpenetration of concealed granite intrusions to deduce the potential for deep mineralization. Based on these results, the JSZF is probably related to mineralization at deep depths that is surrounded by possible ore-forming fluids and materials originating from concealed granite intrusions. According to the maximum coverage depth given in section 4.1, a 3D metallogenic model is established to interpret the deep mineralization potential in the Qingchengzi ore field (Fig. 13). The blue isosurface with a velocity of 3.275 km/s (IV in Fig. 13), denotes the BYGB related mineralization-alteration regions, and the red isosurface with a velocity of 3.375 km/s represents large-scale potential concealed granite intrusive bodies numbered I, II, and III that are related to gold mineralization beneath the Shuangdinggou intrusion, Dadingzi intrusion, XTJPZGB, and BYGB, respectively.

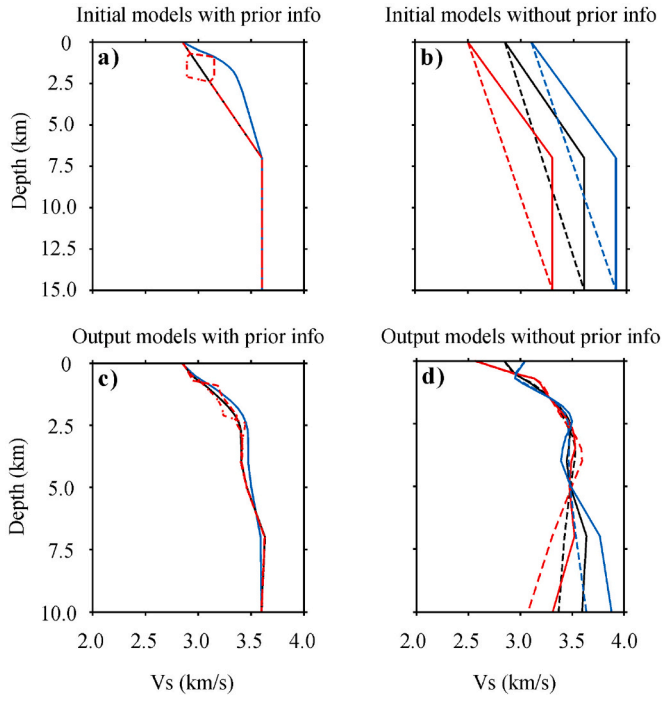

Fig. 12. Inverted average velocity models based on two groups of initial velocity models. a) Initial velocity models of the first group are based on prior information. The blue solid line is the initial velocity model for the direct inversion in section 4, and the black solid line is a linear velocity model. Red dashed lines denote the linear model with low- and high-velocity anomalies at depths of 1.2–2.4 km, respectively. b) Initial velocity models of the second group without prior information. Black, blue, and red solid lines denote the linear initial velocity models with one or two velocity gradients generated without prior information (black lines) and then shift them systematically to generate another two subgroups of higher (blue lines) and lower (red lines) initial velocity models, respectively. c) Inverted average velocity of the first group initial models. d) Inverted average velocity of the second group of initial models. The initial models and their inversion results are shown in the same colour and line type. (For interpretation of the references to colour in this figure legend, the reader is referred to the web version of this article.)

6. Conclusion

In this paper, we have presented the feasibility of ambient noise tomography with a transmissive dense short-period seismic array, QSP array-I, and obtain a 3D shallow crustal velocity structure at depths less than 5.0 km in the Qingchengzi ore field. Using QSP array-I, we establish a subsurface model in the survey area, which reveals the relationship between lithology and stratigraphy, fault structure, concealed granite intrusions, and gold mineralization, and provides evidence for effective deeply buried gold deposits. The JSZF is imaged as deep as 5.0 km and probably contributes to gold mineralization along with low-velocity anomalies interpreted as ore-forming fluids and materials originating from adjacent concealed rocks. Considering that the deposits in the Qingchengzi ore field are all granitoid-related and have a magmatic origin, large-scale potential concealed granite intrusions related to gold mineralization are interpreted to be present beneath the Shuangdinggou intrusion, Dadingzi intrusion, XTJPZGB, and BYGB, which may provide important heat, fluid, and partial source materials for gold mineralization. Combined with the velocity and magnetotelluric results, we present two favorable exploration zones at great depths compared with those of previous shallow geological surveys. One is beneath the BYGB in the northern ore field, and the other is beneath the XTJPZGB in the southern ore field.

This study successfully applies the ambient noise tomography method with an experimental short-period array, QSP array-I, to mineral prospecting at great depths (> 1.5 km) in the Qingchengzi ore field; the QSP array-I provides a new transmissive way to image shallow regional velocity structures. To further provide complete geophysical constraints on gold mineralization in the Qingchengzi ore field (e.g., the structure and geometry of ore-bearing formations at shallow depths), additional data from the second phase of the short-period dense array in the center of the Qingchengzi ore field (QSP array-II) will be integrated in our following work. Moreover, the integration of geophysical, geological, and mineralogical methods would likely provide breakthroughs for mineral prospecting in the future.

Declaration of Competing Interest

We declare that this manuscript has not been previously submitted elsewhere. There are no conflicts of interest.

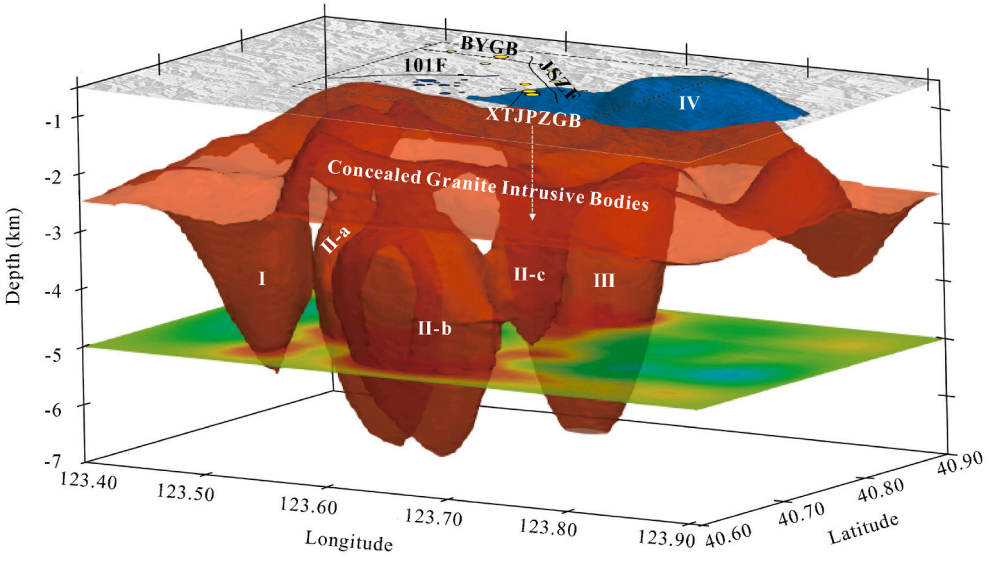

Fig. 13. A 3D metallogenic model of the Qingchengzi ore field. The blue body numbered IV, with an isosurface velocity of 3.275 km/s, denotes the BYGB related mineralization-alteration regions, and the red one, with an isosurface velocity of 3.375 km/s, indicates the potential concealed granite intrusions related to mineralization at the greater depth of the Qingchengzi ore field. Three concealed granite intrusive bodies numbered I, II, and III are beneath the Shuangdinggou intrusion, Dadingzi intrusion, XTJPZGB, and BYGB, respectively. Concealed granite intrusive body II is possibly composed of three subbranches: II-a, II-b, and II-c. Both concealed granite intrusions II-a and II-c connect with intrusion II-b. The velocity slice at a depth of 5.0 km shows that the low-velocity anomalies in the south and north of the ore field extend along the JSZF. (For interpretation of the references to colour in this figure legend, the reader is referred to the web version of this article.)

Acknowledgments

We acknowledge the work carried out by Liaohe Geophysical Exploration Company of Bureau of Geophysical Prospecting INC., China National Petroleum Corporation. Thanks to Seismic Array Laboratory, Institute of Geology and Geophysics, Chinese Academy of Sciences, Southern University of Science and Technology, Guilin University of Technology, Institute of Disaster Prevention, Prof. Zhi Zhang, Drs. Bateer Wu, Guangbing Hou, Zhiming Bai, Yuan Ling, Jincheng Xu, Minfu Huang, Weiyu Dong, Yang He, Long Li and Yuepeng Huang for the contribution in the data acquisition. We appreciate the constructive suggestions from Profs. Tianyu Zheng, Laicheng Miao, Tingjie Yan, Huajian Yao, Yingjie Yang, Yonghua Li, Yong Zheng and Youshan Liu. We also thank Ramon Carbonell, Khalil Motaghi, and an anonymous reviewer for their constructive comments to improve the quality of the manuscript. This work is financially supported by National Key Research and Development Program of China (2016YFC0600101).

Appendix A. Supplementary data

Supplementary data to this article can be found online at https://doi.org/10.1016/j.tecto.2021.228913.

References

Bao, F., Li, Z., Yuen, D.A., Zhao, J., Ren, J., Tian, B., Meng, Q., 2018. Shallow structure of the Tangshan fault zone unveiled by dense seismic array and horizontal-to-vertical spectral ratio method. Phys. Earth Planet. Inter. 281, 46–54.

Bensen, G., Ritzwoller, M., Barmin, M., Levshin, A.L., Lin, F., Moschetti, M., Shapiro, N., Yang, Y., 2007. Processing seismic ambient noise data to obtain reliable broad-band surface wave dispersion measurements. Geophys. J. Int. 169, 1239–1260.

Campillo, M., Roux, P., Romanowicz, B., Dziewonski, A., 2014. Seismic imaging and monitoring with ambient noise correlations. Treatise Geophys. 1, 256–271.

Chang, J.P., de Ridder, S.A., Biondi, B.L., 2016. High-frequency Rayleigh-wave tomography using traffic noise from Long Beach, CaliforniaTomography using traffic noise. Geophysics 81, B43–B53.

Chmiel, M., Roux, P., Bardainne, T., 2016. Extraction of phase and group velocities from ambient surface noise in a patch-array configuration. Geophysics 81, KS231–KS240.

Chmiel, M., Mordret, A., Boué, P., Brenguier, F., Lecocq, T., Courbis, R., Hollis, D., Campman, X., Romijn, R., Van der Veen, W., 2019. Ambient noise multimode Rayleigh and love wave tomography to determine the shear velocity structure above the Groningen gas field. Geophys. J. Int. 218, 1781–1795.

Di, Q., Xue, G., Zeng, Q., Wang, Z., An, Z., 2020. Magnetotelluric exploration of deep-seated gold deposits in the Qingchengzi orefield, Eastern Liaoning (China), using a SEP system. Ore Geol. Rev. 103501.

Du, P., Wu, J., Li, Y., Wang, J., Han, C., Lindsay, M.D., Yuan, H., Zhao, L., Xiao, W., 2020. Imaging karatungk Cu-Ni mine in Xinjiang, Western China with a passive seismic array. Minerals 10, 601.

Duan, X., Zeng, Q., Yang, J., Liu, J., Wang, Y., Zhou, L., 2014. Geochronology, geochemistry and Hf isotope of late Triassic magmatic rocks of Qingchengzi district in Liaodong peninsula, Northeast China. J. Asian Earth Sci. 91, 107–124.

Duan, X., Zeng, Q., Wang, Y., Zhou, L., Chen, B., 2017. Genesis of the Pb-Zn deposits of the Qingchengzi ore field, eastern Liaoning, China: Constraints from carbonate LA-ICPMS trace element analysis and C-O-S-Pb isotopes. Ore Geol. Rev. 89, 752–771.

Dunkin, J.W., 1965. Computation of modal solutions in layered, elastic media at high frequencies. Bull. Seismol. Soc. Am. 55, 335–358.

Fang, H., Zhang, H., 2014. Wavelet-based double-difference seismic tomography with sparsity regularization. Geophys. J. Int. 199, 944–955.

Fang, H., Yao, H., Zhang, H., Huang, Y.-C., van der Hilst, R.D., 2015. Direct inversion of surface wave dispersion for three-dimensional shallow crustal structure based on ray tracing: methodology and application. Geophys. J. Int. 201, 1251–1263.

Hao, L., Zhao, X., Zhao, Y., 2017. Stable isotope characteristics and ore genesis of the baiyun gold deposit, Liaoning Province. J. Jilin Univ. (Earth Sci. Ed.) 47, 442–451.

Herrmann, R.B., 2001. Computer Programs in Seismology-an Overview of Synthetic Seismogram Computation Version 3.1. Department of Earth and Planetary Sciences, St Louis Univ.

Hollis, D., Mcbride, J., Beaupretre, S., Mordret, A., Brenguier, F., Arndt, N., Good, D., 2019. Ambient noise surface wave tomography at the Marathon PGM-Cu deposit, Ontario, Canada. RECORDER. https://csegrecorder.com/articles/view/ambient-noise-surface-wave-tomography-at-the-marathon-pgm-cu-deposit-ont. (Accessed 12 May 2021).

Huang, Y.-C., Yao, H., Huang, B.-S., van der Hilst, R.D., Wen, K.-L., Huang, W.-G., Chen, C.-H., 2010. Phase velocity variation at periods of 0.5–3 seconds in the Taipei Basin of Taiwan from correlation of ambient seismic noise. Bull. Seismol. Soc. Am. 100, 2250–2263.

Lavoué, A., Arndt, N., McBride, J., Mordret, A., Brenguier, F., Boué, P., Courbis, R., Beauprêtre, S., Beard, C., Hollis, D., 2020. Ambient noise Rayleigh and Love wave tomography beneath the sally palladium-copper deposit (Ontario, Canada), SEG Technical Program Expanded Abstracts 2020. Soc. Explor. Geophys. 2075–2079.

Li, Z., Ni, S., Zhang, B., Bao, F., Zhang, S., Deng, Y., Yuen, D.A., 2016. Shallow magma chamber under the Wudalianchi Volcanic Field unveiled by seismic imaging with dense array. Geophys. Res. Lett. 43, 4954–4961.

Lin, W., Wang, Q., Wang, J., Wang, F., Chu, Y., Chen, K., 2011. Late Mesozoic extensional tectonics of the Liaodong Peninsula massif: Response of creust to continebtal lithosphere destruction of the North China Craton. Sci. China Earth Sci. 54, 843–857.

Lin, F., Li, D., Clayton, R.W., Hollis, D., 2013. High-resolution 3D shallow crustal structure in Long Beach, California: Application of ambient noise tomography on a dense seismic arrayNoise tomography with a dense array. Geophysics 78, Q45–Q56.

Liu, Z., Xu, X., Tian, Y., Yang, D., Jiang, Y., Tian, S., Wei, M., 2007. Relationship between sedimentation-exhalation ore-forming process and gold-silver polymetallic mineralization in Qingchengzi area, Liaoning Province. Mineral Deposits 26, 563–571 (in Chinese).

Liu, G., Ai, Y., 1998. Petrological geochemistry and ore-forming conditions of the Xiaotongjiapuzi gold deposit in eastern Liaoning. Mineral Deposits 17, 289–295 (in Chinese).

Liu, G., Ai, Y., 1999. A discussion on some major problems of the Baiyun gold deposit, eastern Liaoning. Mineral Deposits 18, 219–225 (in Chinese).

Liu, G., Ai, Y., 2000. Studies on the mineralization age of Baiyun gold deposit in Liaoning. Acta Petrol. Sin. 16, 627–632 (in Chinese).

Liu, G., Ai, Y., 2002. Study on ore-forming epoch of Xiaotongjiapuzi gold deposit, Liaoning Province. Mineral Deposits 21, 53–57 (in Chinese).

Liu, Y., Niu, F., Chen, M., Yang, W., 2017a. 3-D crustal and uppermost mantle structure beneath NE China revealed by ambient noise adjoint tomography. Earth Planet. Sci. Lett. 461, 20–29.

Liu, Z., Tian, X., Gao, R., Wang, G., Wu, Z., Zhou, B., Tan, P., Nie, S., Yu, G., Zhu, G., 2017b. New images of the crustal structure beneath eastern Tibet from a high-density seismic array. Earth Planet. Sci. Lett. 480, 33–41.

Lo, S., Yao, H., Li, Q., Wang, W., Wan, K., Meng, Y., Liu, B., 2019. High-resolution 3D crustal S-wave velocity structure of the Middle-lower Yangtze River Metallogenic Belt and implications for its deep geodynamic setting. Sci. China Earth Sci. 62, 1361–1378.

Mordret, A., Landès, M., Shapiro, N.M., Singh, S.C., Roux, P., Barkved, O.I., 2013. Near-surface study at the Valhall oil field from ambient noise surface wave tomography. Geophys. J. Int. 193, 1627–1643.

Mordret, A., Landès, M., Shapiro, N.M., Singh, S.C., Roux, P., 2014. Ambient noise surface wave tomography to determine the shallow shear velocity structure at Valhall: depth inversion with a Neighbourhood Algorithm. Geophys. J. Int. 198, 1514–1525.

Mordret, A., Roux, P., Boué, P., Ben-Zion, Y., 2019. Shallow three-dimensional structure of the San Jacinto fault zone revealed from ambient noise imaging with a dense seismic array. Geophys. J. Int. 216, 896–905.

Nakata, N., Chang, J.P., Lawrence, J.F., Boué, P., 2015. Body wave extraction and tomography at Long Beach, California, with ambient-noise interferometry. J. Geophys. Res. Solid Earth 120, 1159–1173.

Niu, M., 2020. Deep Spatial Relationship and Ore Control of Mesozoic Intrusive Rocks in Qingchengzi Mineral Cluster Region. MS dissertation. Jilin University (in Chinese).

Rawlinson, N., Sambridge, M., 2005. The fast marching method: an effective tool for tomographic imaging and tracking multiple phases in complex layered media. Explor. Geophys. 36, 341–350.

Roux, P., Moreau, L., Lecointre, A., Hillers, G., Campillo, M., Ben-Zion, Y., Zigone, D., Vernon, F., 2016. A methodological approach towards high-resolution surface wave imaging of the San Jacinto Fault Zone using ambient-noise recordings at a spatially dense array. Geophys. J. Int. 206, 980–992.

Sabra, K.G., Gerstoft, P., Roux, P., Kuperman, W., Fehler, M.C., 2005. Extracting time-domain Green's function estimates from ambient seismic noise. Geophys. Res. Lett. 32.

Scherzer, O., 1993. The use of Morozov's discrepancy principle for Tikhonov regularization for solving nonlinear ill-posed problems. Computing 51, 45–60.

Schmandt, B., Clayton, R.W., 2013. Analysis of teleseismic P waves with a 5200-station array in Long Beach, California: evidence for an abrupt boundary to Inner Borderland rifting. J. Geophys. Res. Solid Earth 118, 5320–5338.

Shearer, P.M., 2019. Introduction to Seismology. Cambridge university press.

Song, Y., Yang, F., Yan, G., Wei, M., Shi, S., 2016. SHRIMP U-Pb ages and Hf isotopic compositions of Paleoproterozoic granites from the Eastern part of Liaoning Province and their tectonic significance. Acta Geol. Sin. 90, 2620–2636 (in Chinese).

Sun, L., Sun, W., Zhao, G., 1997. Geological characteristics of Xiao-Dong-Jia-Bao-Zi gold-silver deposit of Qing-Cheng-Zi ore field and it source of mineralized matter. Gold 12, 13–18 (in Chinese).

Sun, G., Zeng, Q., Li, T., Li, A., Wang, E., Xiang, C., Wang, Y., Chen, P., Yu, B., 2019. Ore genesis of the Baiyun gold deposit in Liaoning province, NE China: constraints from fluid inclusions and zircon U–Pb ages. Arab. J. Geosci. 12, 299.

Sun, G., Zeng, Q., Zhou, L., Wang, Y., Chen, P., 2020. Trace element contents and in situ sulfur isotope analyses of pyrite in the Baiyun gold deposit, NE China: Implication for the genesis of intrusion-related gold deposits. Ore Geol. Rev. 118, 103330.

Wang, X., Liu, P., Yang, G., Zhang, X., Yi, X., 2010. Analyzing the geological features of the qingchengzi Pb-Zn ore field. Non-Ferrous Min. Metall. 26, 2–6.

Wang, Z., Wang, K., Wei, L., Li, J., Fu, L., 2014. Hydrothermal superposition mineralization and fluid origin of the Gaojiapuzi silver deposit in Liaoning province. Geol. Explor. 50, 1076–1086 (in Chinese).

Wang, Y., Xie, H., Li, D., Shi, Y., Liu, F., Sun, G., Sun, Q., Zhou, G., 2017. Prospecting prediction of ore concentration area exemplified by Qingchengzi Pb-Zn-Au-Ag ore concentration area, eastern Liaoning Province. Mineral Deposits 36, 1–24 (in Chinese).

Wang, G., Tian, X., Guo, L., Yan, J., Lyu, Q., 2018. High-resolution crustal velocity imaging using ambient noise recordings from a high-density seismic array: An example from the Shangrao section of the Xinjiang basin, China. Earthq. Sci. 1.
Wang, Z., Jiang, M., Peng, L., Cheng, S., 2020. The application of aeromagnetotelluric survey technology to Dandong area, Liaoning Province. Geophys. Geochem. Explor. 44, 734–741 (in Chinese).
Wei, Y., Tian, X., Duan, Y., Tian, X., 2018. Imaging the topography of crust–mantle boundary from a high-density seismic array beneath the middle-lower Yangtze River, Eastern China. Seismol. Res. Lett. 89, 1690–1697.
Wu, F., Lin, J., Wilde, S.A., Yang, J., 2005a. Nature and significance of the early cretaceous giant igneous event in eastern China. Earth Planet. Sci. Lett. 233, 103–119.
Wu, F., Yang, J., Wilde, S.A., Zhang, X., 2005b. Geochronology, petrogenesis and tectonic implications of Jurassic granites in the Liaodong Peninsula, NE China. Chem. Geol. 221, 127–156.
Wu, J., Zhi, Q., Deng, X., Wang, X., Yang, Y., Zhang, J., Dai, P., 2020. Exploration of deep geological structure of baiyun gold deposit in eastern liaodong provience with TEM. Earth Sci. 45, 4027–4037.
Xue, C., Chen, Y., Lu, Y., Li, H., 2003. Metallogenic epochs of Au and Ag deposits in Qingchengzi ore-clustered area, eastern Liaoning Province. Mineral Deposits 22, 177–184 (in Chinese).
Yang, F., 2019. Metallogenic Characteristics, Deposit Genesis, Metallogenic Mode and Regularity of the Gold Polymetallic Deposit in Qingchengzi Deposit-Concentrated Area, Liaoning, PhD dissertation. Jlin University (in Chinese).
Yang, J., Wu, F., Wilde, S.A., 2003. A review of the geodynamic setting of large-scale late Mesozoic gold mineralization in the North China Craton: an association with lithospheric thinning. Ore Geol. Rev. 23, 125–152.
Yang, J., Wu, F., Lo, C., Chung, S., Zhang, Y., Simon, A.W., 2004. Deformation age of Jurassic granites in the Dandong area, eastern China: 40Ar/30Ar geochronological constraints. Acta Geol. Sin. 20, 1205–1214.
Yang, J., Wu, F., Chung, S., Lo, C., 2008. The extensional geodynamic setting of early cretaceous granitic intrusions in the Eastern North China Craton: evidence from laser ablation 40Ar/39Ar dating of K-bearing minerals. Acta Geol. Sin. 24, 1175–1184.
Yao, H., van Der Hilst, R.D., De Hoop, M.V., 2006. Surface-wave array tomography in SE Tibet from ambient seismic noise and two-station analysis—I. Phase velocity maps. Geophys. J. Int. 166, 732–744.
Yao, H., Beghein, C., Van Der Hilst, R.D., 2008. Surface wave array tomography in SE Tibet from ambient seismic noise and two-station analysis-II. Crustal and upper-mantle structure. Geophys. J. Int. 173, 205–219.
Yu, G., Chen, J., Xue, C., Chen, Y., Chen, F., Du, X., 2009. Geochronological framework and Pb, Sr isotope geochemistry of the Qingchengzi Pb–Zn–Ag–Au orefield, Northeastern China. Ore Geol. Rev. 35, 367–382.
Yu, G., Xu, T., Liu, J., Ai, Y., 2020. Late Mesozoic extensional structures and gold mingralization in Jiaodong Peninsula, eastern North China Craton: the inspiration from ambient noise tmography with a dense sesmic array. Chin. J. Geophys. (in Chinese) 63, 1878–1893.
Zeng, Q., Chen, R., Yang, J., Sun, G., Yu, B., Wang, Y., Chen, P., 2019. The metallogenic characteristics and exploring ore potential of the gold deposits in eastern Liaoning Provience. Acta Petrol. Sin. 35, 1939–1963.
Zhang, P., Yang, H., Li, B., Kou, L., Yang, F., 2016. Ore source, ore-forming age and geodynamic setting of Yaojiagou molybdenum deposit in Qingchengzi ore-clustered area, Eastern Liaoning Province. J. Jilin Univ. (Earth Sci. Ed.) 46, 1684–1696.
Zhang, Z., Deng, Y., Yao, J., Zong, J., Chen, H., 2021. An array based seismic image on the Dahutang deposit, South China: Insight into the mineralization. Phys. Earth Planet. Inter. 310, 106617.
Zhu, R., Sun, W., 2021. The big mantle wedge and decratonic gold deposits. Sci. China Earth Sci. 64, 1–13.
Zhu, R., Fan, H., Li, J., Meng, Q., Li, S., Zeng, Q., 2015. Decratonic gold deposits. Sci. China Earth Sci. 58, 1523–1537.